PAPER

An L-shaped and bending-torsion coupled beam for self-adaptive vibration energy harvesting

To cite this article: Yi Huang *et al* 2023 *J. Phys. D: Appl. Phys.* **56** 284001

View the article online for updates and enhancements.

An L-shaped and bending-torsion coupled beam for self-adaptive vibration energy harvesting

Yi Huang[1,2] ![ORCID]**, Guobiao Hu**[4] ![ORCID]**, Chaoyang Zhao**[2]**, Baoping Tang**[1,*] ![ORCID]**, Xiaojing Mu**[3] ![ORCID] **and Yaowen Yang**[2,*] ![ORCID]

[1] College of Mechanical and Vehicle Engineering, Chongqing University, Chongqing 400044, People's Republic of China
[2] School of Civil and Environmental Engineering, Nanyang Technological University, 50 Nanyang Avenue, Singapore 639798, Singapore
[3] Key Laboratory of Optoelectronic Technology & Systems Ministry of Education, International R & D center of Micro-nano Systems and New Materials Technology, Chongqing University, Chongqing 400044, People's Republic of China
[4] Internet of Things Thrust, The Hong Kong University of Science and Technology (Guangzhou), Guangzhou 511400, People's Republic of China

E-mail: bptang@cqu.edu.cn and cywyang@ntu.edu.sg

Abstract

Vibration energy harvesting is promising for powering wireless sensor networks for mechanical equipment monitoring. Considering the broadband feature of ambient vibrations, a novel L-shaped self-adaptive piezoelectric energy harvester (LSA-PEH) with a slider is proposed. A linearized mathematical model of the LSA-PEH is established to obtain the relationship between its resonant frequency and the slider position. The maximum resonant frequency that can be achieved by the LSA-PEH is predicted based on the linearized model. The corresponding condition is to fix the slider at around 0.08 m, which is a nodal point. Moreover, the theoretical model explains why the slider moves back and forth when the excitation frequency is 40 Hz. Experimental results show that the slider of the proposed LSA-PEH can passively relocate its position to adjust its resonant frequency and maintain resonance. By the same criteria, the bandwidth of the proposed LSA-PEH is increased by 350% compared to a conventional L-shaped beam harvester.

Keywords: energy harvesting, self-adaptive, bending-torsion coupling, L-shaped beam

(Some figures may appear in colour only in the online journal)

1. Introduction

Wireless sensor networks (WSN) [1–3] for structural health monitoring provide unique advantages in the application of the mechanical equipment, which wired systems cannot access, such as gearboxes, axle boxes, etc. However existing issues, such as clock synchronization, and energy supply, limit the development of WSN systems. In particular, since many sensor nodes need be deployed at difficult-to-reach or dangerous places, using battery-power solutions would limit their service lifetime. To prolong their lifetime, some researchers focused on developing low-power consumption circuits [4], improving the topology control strategies [5], and designing more intelligent sleep schedules [6]. In brief, these methods are all based on the idea of reducing the energy consumption

---

* Authors to whom any correspondence should be addressed.

of sensor nodes. However, the energy depletion problem is only deferred but never solved by the above means. Perpetual power supply solutions have to be developed to solve the above problem at its root. From this point of view, harnessing energy from the ubiquitous vibrations in the ambient environment is a promising solution [7–9].

A traditional and simplest energy harvester can be obtained by attaching a piezoelectric patch to a cantilevered beam. Structural resonance occurs when the ambient vibration frequency matches the resonant frequency of this piezoelectric energy harvester (PEH). Thus, a large amount of power output is produced. However, the output magnitude of the PEH decreases dramatically if the ambient excitation frequency deviates from its resonant frequency. In practical applications, environmental vibration energy usually spreads over a wide frequency range. Therefore, researchers have devoted numerous efforts to widening the operating bandwidths of vibration energy harvesters.

Common approaches for broadband energy harvesting include introducing an array of PEHs with independent frequencies and designing multi-degree-of-freedom (MDOF) PEHs. Each PEH unit has a different narrow bandwidth in the multi-array approach; thereby, the total bandwidth is considerably large [10]. The principle of the MDOF design strategy is to tune two or multiple natural frequencies close to each other to form a wide frequency range for energy harvesting. To give a few examples, Xiao *et al* [11] proposed a novel PEH that was comprised of multiple piezoelectric beams. They provided a guideline for tuning the operating bandwidth based on the theoretical analysis. Li *et al* [12] designed a novel sandwich PEH and adjusted the resonance to realize energy harvesting over a wide frequency range.

In addition to the aforementioned methods, nonlinear elements such as nonlinear springs, magnets, and buckling beams, have also been introduced to widen the operating bandwidth of PEHs. Zou *et al* [13] developed an energy harvesting system that consisted of a pre-compressed spring, a bearing, and a raceway to improve the dynamic performance. Haghighi *et al* [14] investigated a piezoelectric beam array coupled with a magnet theoretically and experimentally. Xie *et al* [15] proposed a T-shaped PEH based on the internal resonance mechanism and multimodal techniques. The results indicated the T-shaped PEH could achieve 1:3 internal resonance. Nonlinear energy harvesters at high-energy orbits exhibit superior performance over a broadband frequency range. However, the performance will dramatically deteriorate if the nonlinear energy harvesters jump to low-energy orbits.

Besides, the self-adaptive technology is another potential solution to address the narrow-bandwidth issue. A self-adaptive PEH is expected to maintain resonance without any human intervention by automatically adjusting its resonant frequency to match the ambient excitation. Self-adaptive energy harvesting was firstly investigated by Miller *et al* [16]. They developed a clamped-to-clamped beam-mass system with self-tuning capability. The system kept at the resonant state as the excitation frequency swept up or down. Lan *et al* [17] designed a similar system but with a clamped-free

boundary condition. The experimental results showed that with the increase of the excitation frequency, the sliding mass passively moved along the beam and stopped at different positions to activate the second-mode resonance.

In addition to the conventional PEHs working in the bending mode, Abdelkefi *et al* [18] proposed a T-shaped PEH and pointed out that due to the bending–torsion coupling effect, the T-shaped PEH produced 30% more power output than a cantilever beam PEH. Similar to the T-shaped PEH, researchers have studied L-shaped PEHs for their simple structure and ease of production [19–21]. Cao *et al* [22] points out the not in-plane vibration of L-shaped will significant increase the system output, which indicates that the bending-torsion vibration of the system can generate high voltage output.

Inspired by the self-adaptive idea and the benefits of L-shaped beams, this paper proposes an L-shaped self-adaptive PEH (LSA-PEH) by introducing a moveable mass, i.e. a slider, to enhance broadband energy harvesting performance. This work aims to reveal the relationship between the frequency response of the L-shaped beam and the slider location. It is found that the slider helps the system generate high output when excitation frequency varies. The system maximum 2nd-order resonant frequency is fixed with the changing slider mass.

The rest of the paper is organized as follows: section 2 introduces the design and modeling of the LSA-VEH. Section 3 presents the numerical results of the LSA-VEH based on the theoretical model developed in section 2. Section 4 presents the experimental results and discussions. Conclusions are summarized in section 5.

2. Design and modeling of the harvester

2.1. Working principle

As shown in figure 1, the proposed LSA-PEH consists of an L-shaped piezoelectric beam and a movable mass, i.e. a slider. A force analysis during the vibration of the beam is first conducted to explain its working principle [23]. As depicted in figure 2, the inertial force applied on the slider is $F_i = -ma$ when the beam vibrates at an acceleration of *a, m* is the mass of the slider. The inertial force is always opposite to the direction of the beam's motion. In addition to the inertial force, F_g, the normal force (F_n) and the friction force (F_f) applied to the slider are also depicted in figure 2. Obviously, the direction of the total force F_T (the combination of F_i, F_n, and F_g) is always along the beam and bigger than the friction F_f. Therefore, the force along the beam length direction is nonzero, the slider will move along the beam during the vibration.

When there is no external excitation, the LSA-PEH at static has a tilt angle θ, as shown in figure 2(a), due to the initial deformation under the gravity effect. In the beginning, before the vibration amplitude of the beam exceeds the horizontal dashed line, the total force F_T (as shown in equation (1)) applied on the slider always points to the free end. According to equation (1), when the slider gets closer to the resonant position, the tilt angle θ increases, making the total force
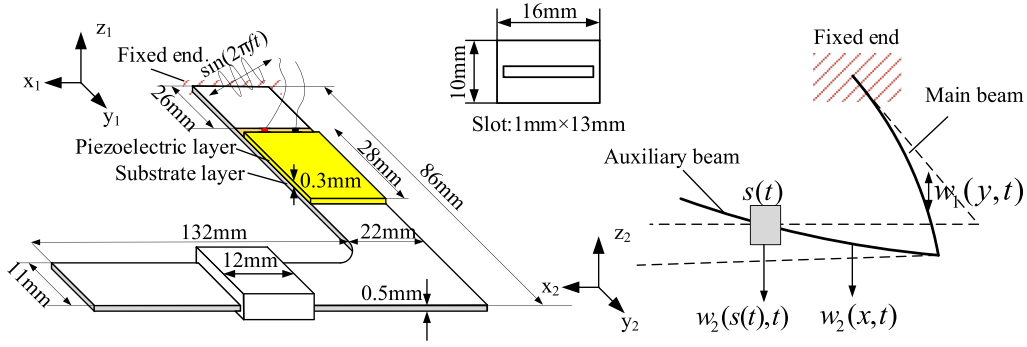
Figure 1. Model diagram and the geometric dimensions of the proposed LSA-PEH.
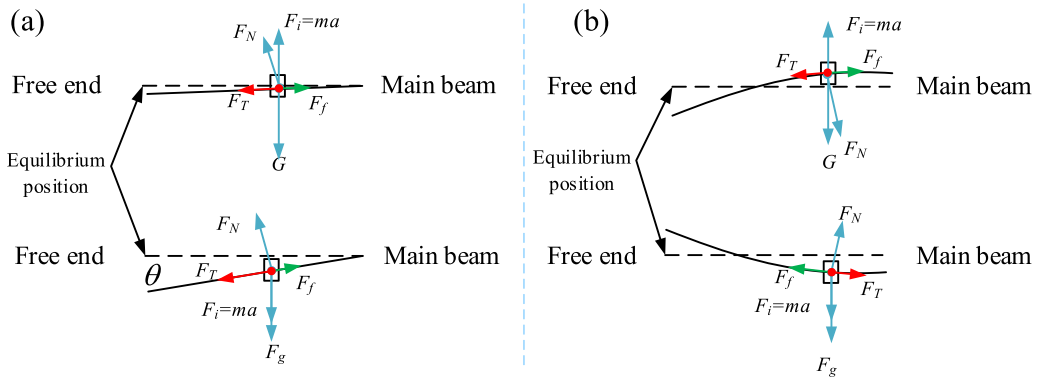

Figure 2. Force analysis (a) at the beginning; (b) at the stable position (the 2nd vibration mode).

applied to the slider larger. Thus, the acceleration magnitude of the slider along the beam also increases. The slider will be quickly dragged to the resonant position, where the beam reaches the largest amplitude response. The slider finally stops at or near the position where the L-shaped beam activates its second-mode resonance,

$$F_\text{T} = (F_\text{g} + F_\text{i}) \sin\theta + \frac{F_\text{g} + F_\text{i}}{\cos\theta} \sin\theta - F_\text{f}. \tag{1}$$

The following discussions are to explain why the second mode is activated rather than the first mode. In the fundamental mode, the slider always moves to the free end until it slips off the beam. This is because the beam has an initial downward inclination under the gravitation effect. Due to this initial bias, the maximum magnitude of the total force F_T in equation (1) is larger when the beam is below the horizontal line than when the beam is above the horizontal line. In other words, the slider will move faster when the beam is below the horizontal line. By any means, the slider will finally slip off the beam. The force acting on the slider in the second-order mode vibration is depicted in figure 2(b). Even though there is still a tilt angle θ, it is small, so $\sin\theta$ is nearing zero in equation (2). In the case of such a slight angle, the static friction should be considered since total force F_T also becomes pretty small. The tangential force along the beam length direction will eventually be balanced. Thus, the slider will stop at this position,

$$(F_\text{g} - F_\text{i}) \sin\theta - F_\text{f} = F_\text{T}. \tag{2}$$

2.2. Mathematical modeling

The natural frequencies of the LSA-PEH can be calculated by assuming the slider is fixed on the beam. The modal shape of the system is assumed as follows:

$$\phi_1(y) = a_1 \cosh\alpha_1 y + b_1 \sinh\alpha_1 y + c_1 \cos\alpha_1 y + d_1 \sin\alpha_1 y,$$
$$\phi_2(x) = a_2 \cosh(\alpha_2(x-s)) + b_2 \sinh(\alpha_2(x-s))$$
$$+ c_2 \cos(\alpha_2(x-s)) + d_2 \sin(\alpha_2(x-s)), x > s$$
$$\phi_3(x) = a_3 \cosh\alpha_2 x + b_3 \sinh\alpha_2 x + c_3 \cos\alpha_2 x$$
$$+ d_3 \sin\alpha_2 x, x < s$$
$$\varphi(y) = a_4 \cos\beta y + b_4 \sin\beta y. \tag{3}$$

where $\alpha_i^4 = \frac{\omega^2 \rho_i A_i}{E_i I_i}$, $\beta^2 = \frac{\omega^2 J_1}{G I_1}$, $\rho_i, A_i, E_i, I_i, G \text{and} J_i$, respectively, denote the volume density, the cross-sectional area, the elastic modulus, the inertia moment, the shear modulus, and the rotary inertia of the beam. ω is the resonant frequency of the LSA-PEH, s represents the location of the slider in the auxiliary beam. The subscript $i = 1$ or 2 denotes the main or auxiliary beam.

The boundary conditions of the system are:

$$\phi_1(0) = 0, \phi_1'(0) = 0, \varphi(0) = 0 \tag{4}$$

$$E_2 I_2 \phi_2''(L_2) = 0, E_2 I_2 \varphi_2'''(L_2) = 0 \tag{5}$$

The continuity conditions at the connection between the two beams require:

$$\phi_1(L_1) = \phi_3(0), \varphi(L_1) = \phi_3(0) \tag{6}$$

$$GI_{\mathrm{p}}\varphi(L_2) = E_2I_2\phi_3(0) \tag{7}$$

$$E_1I_1\phi_1(L_1) = 0, E_1I_1\phi_1'''(L_1) = E_2I_2\phi_3'''(0) \tag{8}$$

where I_{p} denote the polar inertia moment of the main beam.

Similarly, the continuity conditions at the position of the slider can be expressed as

$$\phi_2{}^-(s) = \phi_3{}^+(s), \phi_2'{}^-(s) = \phi_2'{}^+(s),$$

$$E_2I_2\phi_2''{}^-(s) = E_2I_2\phi_3''{}^+(s),$$

$$E_2I_2\phi_2'''{}^-(s) - E_2I_2\phi_2'''{}^+(s) = m\ddot{\phi}_2(s) \tag{9}$$

Substituting equation (1) into all the boundary conditions yields:

$$
\begin{cases}
a_1 + c_1 = 0 \\
b_1 + d_1 = 0 \\
a_4 = 0 \\
a_2 \cos h(\alpha_2(L_2-s)) + b_2 \sin h(\alpha_2(L_2-s)) - c_2 \cos(\alpha_2(L_2-s)) - d_2 \sin(\alpha_2(L_2-s)) = 0 \\
a_2 \sin h(\alpha_2(L_2-s)) + b_2 \cos h(\alpha_2(L_2-s)) + c_2 \sin(\alpha_2(L_2-s)) - d_2 \cos(\alpha_2(L_2-s)) = 0 \\
a_1 \cos h\alpha_1 L_1 + b_1 \sin h\alpha_1 L_1 + c_1 \cos \alpha_1 L_1 + d_1 \sin \alpha_1 L_1 = a_3 + c_3 \\
a_4 \cos \beta L_1 + b_4 \sin \beta L_1 = \alpha_2 b_3 + \alpha_2 d_3 \\
-a_4 GI_{\mathrm{p}}\beta \sin \beta L_2 + b_4 GI_{\mathrm{p}}\beta \cos \beta L_2 = a_2 E_2 L_2 - c_2 E_2 L_2 \\
a_1 \cos h\alpha_1 L_1 + b_1 \sin h\alpha_1 L_1 - c_1 \cos \alpha_1 L_1 - d_1 \sin \alpha_1 L_1 = 0 \\
a_1 \alpha_1^3 E_1 I_1 \sin h\alpha_1 L_1 + b_1 \alpha_1^3 E_1 I_1 \cos h\alpha_1 L_1 + c_1 \alpha_1^3 E_1 I_1 \sin \alpha_1 L_1 - d_1 \alpha_1^3 E_1 I_1 \cos \alpha_1 L_1 = b_3 E_2 I_2 \alpha_2^3 - d_3 E_2 I_2 \alpha_2^3 \\
a_3 \cos h\alpha_2 s + b_3 \sin h\alpha_2 s + c_3 \cos \alpha_2 s + d_3 \sin \alpha_2 s = a_2 + c_2 \\
a_3 \sin h\alpha_2 s + b_3 \cos h\alpha_2 s - c_3 \sin \alpha_2 s + d_3 \cos \alpha_2 s = b_2 + d_2 \\
a_3 \cos h\alpha_2 s + b_3 \sin h\alpha_2 s - c_3 \cos \alpha_2 s - d_3 \sin \alpha_2 s = a_2 - c_2 \\
a_3 \alpha_2^3 \sin h\alpha_2 s + b_3 \alpha_2^3 \cos h\alpha_2 s + c_3 \alpha_2^3 \sin \alpha_2 s - d_3 \alpha_2^3 \cos \alpha_2 s - b_2 \alpha_2^3 + d_2 \alpha_2^3 = -\dfrac{m\omega^2}{E_2 I_2}(a_2 + c_2)
\end{cases}
\tag{10}
$$

Equation (10) can be reformulated into the matrix form:

$$\mathbf{H}(\omega)\mathbf{q} = 0 \tag{11}$$

where $\mathbf{q} = [a_1\ b_1\ c_1\ d_1\ a_2\ b_2\ c_2\ d_2\ a_3\ b_3\ c_3\ d_3\ a_4\ b_4]^{\mathrm{T}}$, $\mathbf{H} = \begin{pmatrix} \mathbf{H}_1 & \mathbf{H}_2 \\ \mathbf{H}_3 & \mathbf{H}_4 \end{pmatrix}_{14 \times 14}$. The elements in $\mathbf{H}$ are given in the appendix.

By solving $\det(\mathbf{H}) = 0$, the natural frequencies and modal shapes of the L-shaped beam with a slider can be obtained.

3. Numerical results

Numerical results are given in this section to analyze the frequency response of the L-shaped beam when the sliding mass is fixed at different positions. The system parameters of the fabricated physical prototype are listed in table 1. The geometric dimensions are illustrated in figure 1. The slider is manufactured using a 3D printer. A screw is stuck on the top of the slider to adjust its mass. The total mass of the slider used in the experiment is 3.8 g.

Table 1. The system parameters of the prototyped LSA-PEH.

| L-shaped beam		Piezoelectric patch	
Parameters	Value	Parameters	Value
Density $\rho_1(\rho_2)$ (kg m^{-3})	2700	Density (kg m^{-3})	5440
Young modulus $E_1(E_2)$ (Gpa)	69.5	Young modulus E_{p} (Gpa)	30.336
Shear modulus(G) (Gpa)	26.128	Shear modulus G_{p} (Gpa)	5.515

To first investigate the dynamic characteristics of the proposed LSA-PEH from a qualitative perspective, the slider is fixed on the auxiliary beam (as shown in figure 1). The position of the slider ranges from 0.035 m to 0.1 m. Subsequently, the slider mass is varied to study its effect on the dynamics of the proposed LSA-PEH. The numerical results in fundamental eigenfrequency are demonstrated in figure 3.

According to the numerical results, the fundamental frequency of the LSA-PEH varies from 9 –15 Hz (mass = 3.8 g). Theoretically speaking, the frequency tunable bandwidth is
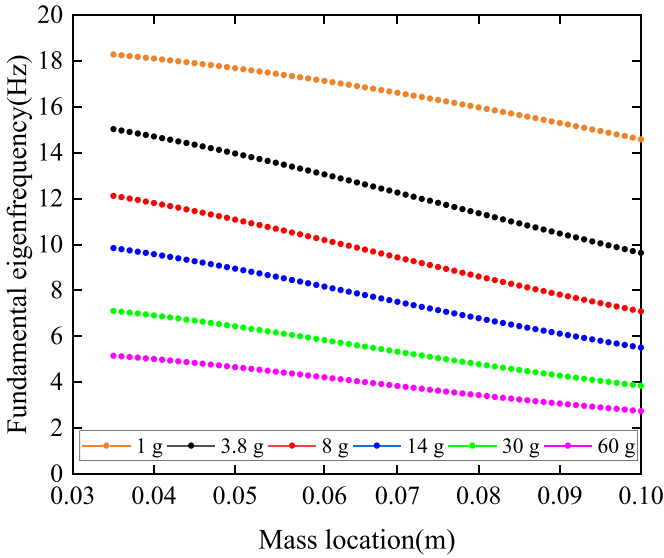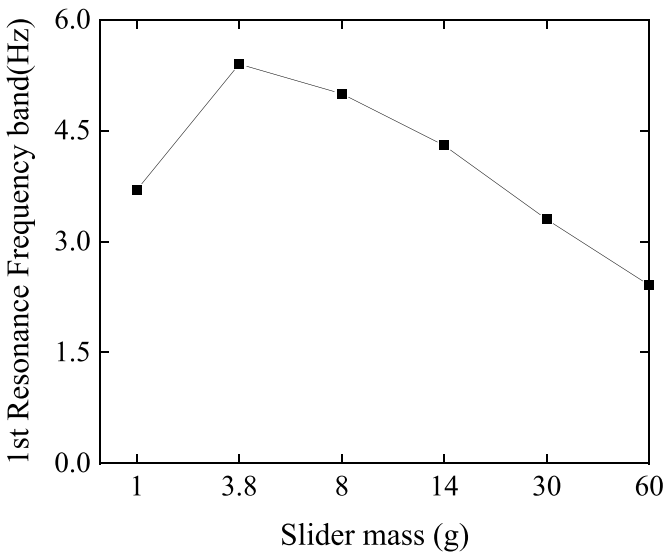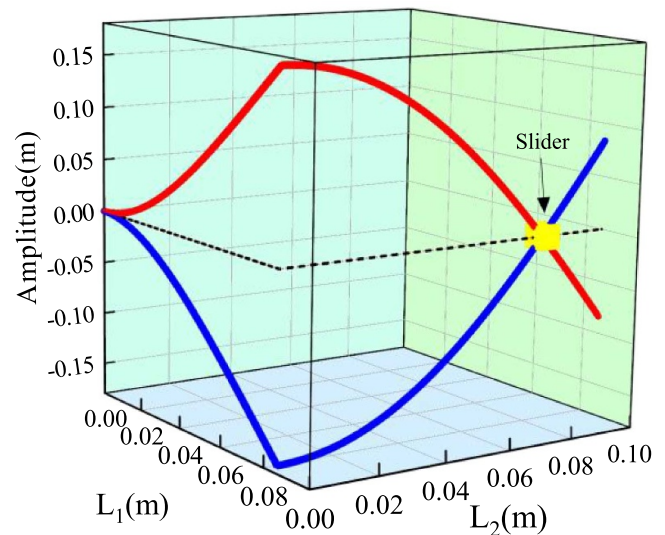
Figure 3. The fundamental eigenfrequency of the proposed LSA-PEH versus the position of the slider with different masses: 1 g, 3.8 g, 8 g, 14 g, 30 g, 60 g.
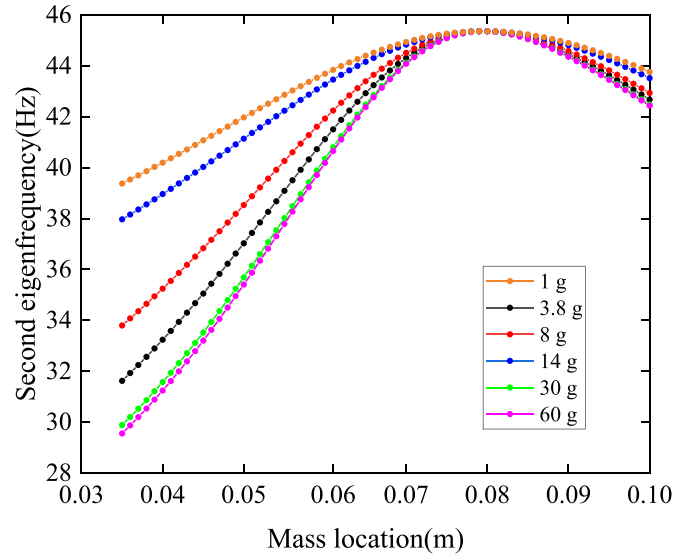
Figure 5. The second eigenfrequency of the proposed LSA-PEH versus the position of the slider with different masses: 1 g, 3.8 g, 8 g, 14 g, 30 g, 60 g.

Figure 4. Fundamental resonance frequency bandwidth evolution of the proposed LSA-PEH with the change of the slider mass.


Figure 6. The second-order modal shape of the LSA-PEH with a point mass fixed at ≈0.08 m.

about 6 Hz. The fundamental frequency decreases with the mass moving towards the free end. On the other hand, the fundamental frequency of the LSA-PEH also decreases with increasing the mass of the slider. Figure 4 reveals that the frequency tunable bandwidth first increases with the increase of the slider mass. The frequency tunable bandwidth reaches a maximum of about 6 Hz when the slider the mass is around 3.8 g. After the slider mass exceeds 3.8 g, the frequency tunable bandwidth starts to decrease.

The numerical results in 2nd-order resonant frequency are demonstrated in figure 5. The 2nd-order resonant frequency of the LSA-PEH can vary from 29.5 Hz to 45.3 Hz when the slider moves along the auxiliary beam. The 2nd-order resonant frequency of the LSA-PEH is fluctuating with the gravity

of the mass increasing. It is worth noting that regardless of the mass change, the 2nd-order resonant frequency of the LSA-PEH remains at 45.3 Hz if the slider (point mass) is fixed at the specific position (0.08 m). This is because the 2nd-order resonant frequency of the L-shaped beam without the slider is just 45.3 Hz. As demonstrated in figure 6, this specific position (0.08 m) is just a node point, i.e. the displacement amplitude is always 0. Therefore, attaching any mass at that specific position will not alter the modal shape of the L-shaped beam at all.

As revealed in figure 7, the 2nd-order resonant frequency bandwidth fluctuates with the increase of the sliding mass. Comparing with the fundamental frequency, the frequency band reaches maximum when the sliding mass is 60 g, which
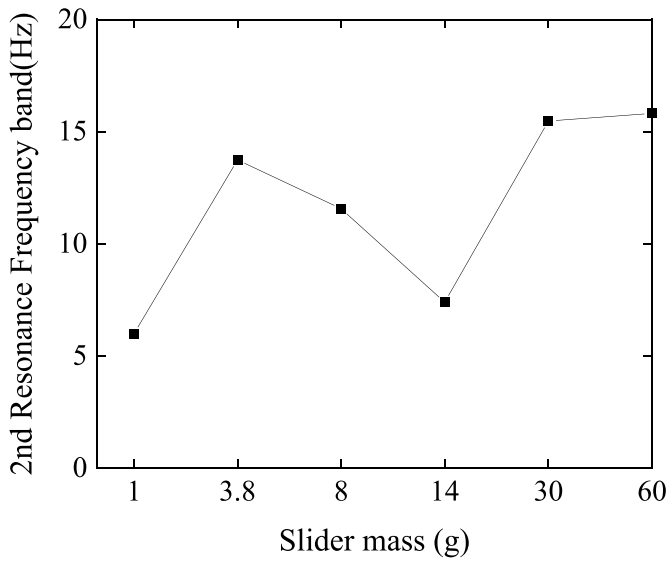
Figure 7. 2nd-order resonant frequency bandwidth evolution of the proposed LSA-PEH with the change of the slider mass.

Figure 8. Experimental setup.

indicates that the 2nd-order resonant frequency band increases more than the fundamental frequency. When the sliding mass increases from 30 g to 60 g, the bandwidth increase is negligible. Moreover, the friction between the slider and the beam cannot be ignored in case of using a large sliding mass. For the above reasons, a 3.8 g slider is chosen to achieve a large bandwidth and keep it lightweight.
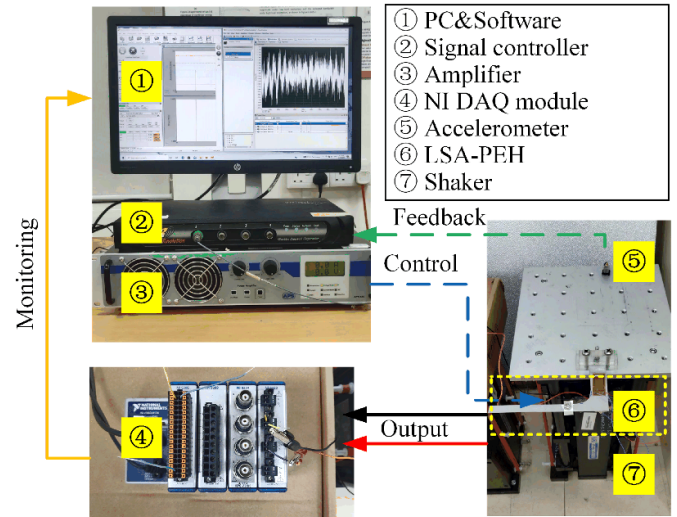
4. Experimental results and discussion

4.1. Experimental setup

The experimental setup is illustrated in figure 8. The L-shaped beam is made of aluminum. A piezoelectric transducer (MFC, M2814) is bounded at the root of the main beam using epoxy glue (DP-460, 3 M Scotch-Weld). The whole system is mounted on the vibration shaker (APS 400) driven by an amplifier (APS 125). An accelerometer is secured on the shaker to provide feedback to the signal controller (VR 9500). The voltage output of the LSA-PEH is measured by a DAQ module (NI 9229) and recorded by the NI SignalExpress software.

4.2. Frequency response

4.2.1. In the fundamental resonant frequency.
The slider is placed near the main beam in the fundamental resonant experiments. The excitation frequency is increased from 11 to 14 Hz to validate the analysis in section 2.1. The voltage response is shown in figure 9. There is a little distance between the initial position of the slider and the resonant position when the excitation frequency is 11 and 12 Hz, so the system output first keeps stable for a short time. After the mass slides to the resonant position, the voltage output reaches maximum. However, the slider is out-of-balance and slips away from the resonant position and off the beam eventually. The above result and

the observations in the experiment all proved that the fundamental vibration mode of the L-shaped beam does not support the activation of the self-adaptivity but will only lead to the slip-off of the slider.
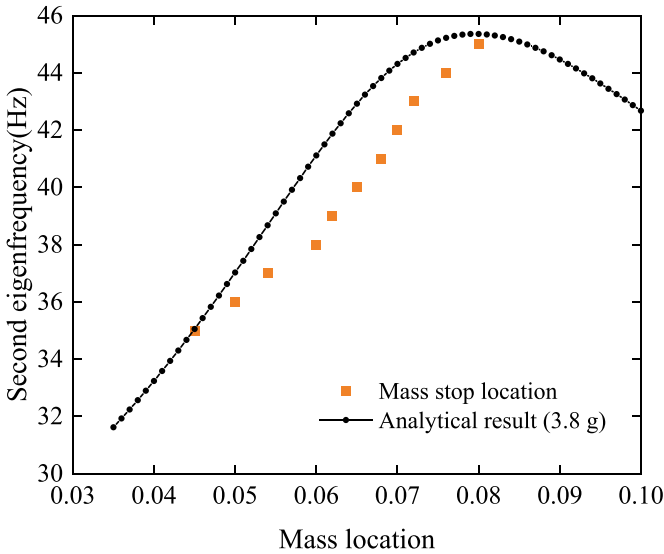
4.2.2. In the second resonant frequency.
In the experiment, the excitation frequency of the shaker was increased from 35 Hz to 45 Hz, according to the simulation results. The starting position of the slider was set at 0.045 m each time. The resonant frequency of the LSA-PEH changed when the slider passively moved and stopped at different positions. The recorded results are presented in figure 10. It can be seen that the natural frequencies measured in the experiment are basically consistent with the predictions of the simulation. The discrepancy might originate from the neglect of the piezoelectric transducer and the gravity effect in the theoretical modeling.

When the excitation frequency varies from 35 Hz to 45 Hz, the voltage output responses of the LSA-PEH are shown in figure 11. The acceleration level is fixed at 0.8*g* (*g* is the gravitational constant). It is clearly observed that the proposed LSA-PEH can automatically adjust the location of the slider from the starting position to the resonant position. The system is able to maintain resonance and produce considerably large voltage output over the frequency range from 35 Hz to 44 Hz. As discussed in the previous section, there is a specific position called the modal node. When the slider moves to that position ($\approx$0.08 m) around 45 Hz, its vibration amplitude is negligible. However, due to the tilt caused by the gravitational effect, the slider tends to move to the free end. Moreover, the excitation from the shaker forced the slider to move toward the free end. Therefore, the voltage output at 45 Hz first increased to a maximum and then decreased rapidly as the slider slipped off the beam.

In figure 11(f), we note that when the excitation frequency is 40 Hz, the slider cannot stably stop at a certain position but floats around there. Figure 2(b) depicts an ideal situation in which the slider can adjust its location automatically.

J. Phys. D: Appl. Phys. **56** (2023) 284001

Y Huang *et al*
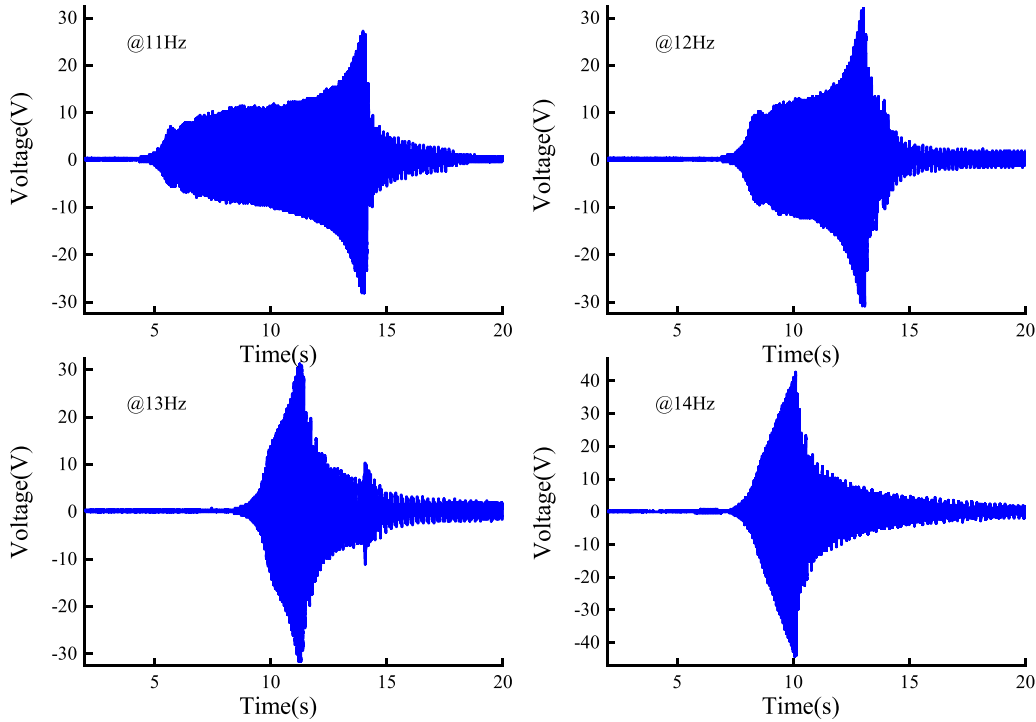
Figure 9. Voltage output responses of the proposed LSA-PEH when the excitation frequency varies from 11 Hz to 14 Hz.

Figure 10. The second resonant frequency of the LSA-PEH versus the slider position: theoretical result (solid-line with dots) and experimental result (square scatters).

However, the slider cannot always stop at the expected position in the practical test. Whether the slider can stop or not depends on whether the friction force can balance the tangential force along the beam length or not. Obviously, a large tilt angle of the slider, i.e. the slope of the auxiliary beam at the slider location, leads to a large tangential force, making it difficult for the slider to stop. To explain the fluctuation phenomenon in figure 11(f), we plotted the slope of the auxiliary beam at the

position where the slider stops in figure 12 by taking the first-order derivative of the modal shape function of the L-shaped beam. It can be seen in figure 12 that the tilt angle of the slider reaches the maximum for the case when its resonant frequency is 41 Hz. Therefore, it can be predicted that it will be the most difficult for the slider to stop at the expected position around 41 Hz. Though there is a minor discrepancy between the theoretical prediction (41 Hz) and the experimental result (40 Hz), considering many uncertainties in the experiment, the above discussion gives a reasonable explanation for the fluctuation phenomenon in figure 11(f).

4.3. Power output result

The power output of the proposed LSA-PEH is compared to that of a conventional L-shaped PEH with a mass fixed at 0.06 m. By sweeping the frequency from 35 Hz to 45 Hz, the power output of the conventional one was recorded. The sweeping rate was 6 Hz min^{-1}. A load resistance of 100 kΩ was used for both harvesters. The results are compared in figure 13. For the conventional L-shaped PEH, the maximum power output occurs when the excitation frequency reaches 38.1 Hz. For the proposed LSA-PEH, the slider passively moved to the position of 0.06 m when the excitation frequency was 38 Hz. The power output of the LSA-PEH is not as high as that of the L-shaped PEH in this case because the collision between the beam and slider consumes additional energy. The power output of the proposed LSA-PEH gradually decreases when the excitation frequency increases and the slider relocates its position. Its power output drops to 0.5 mW at 44 Hz.
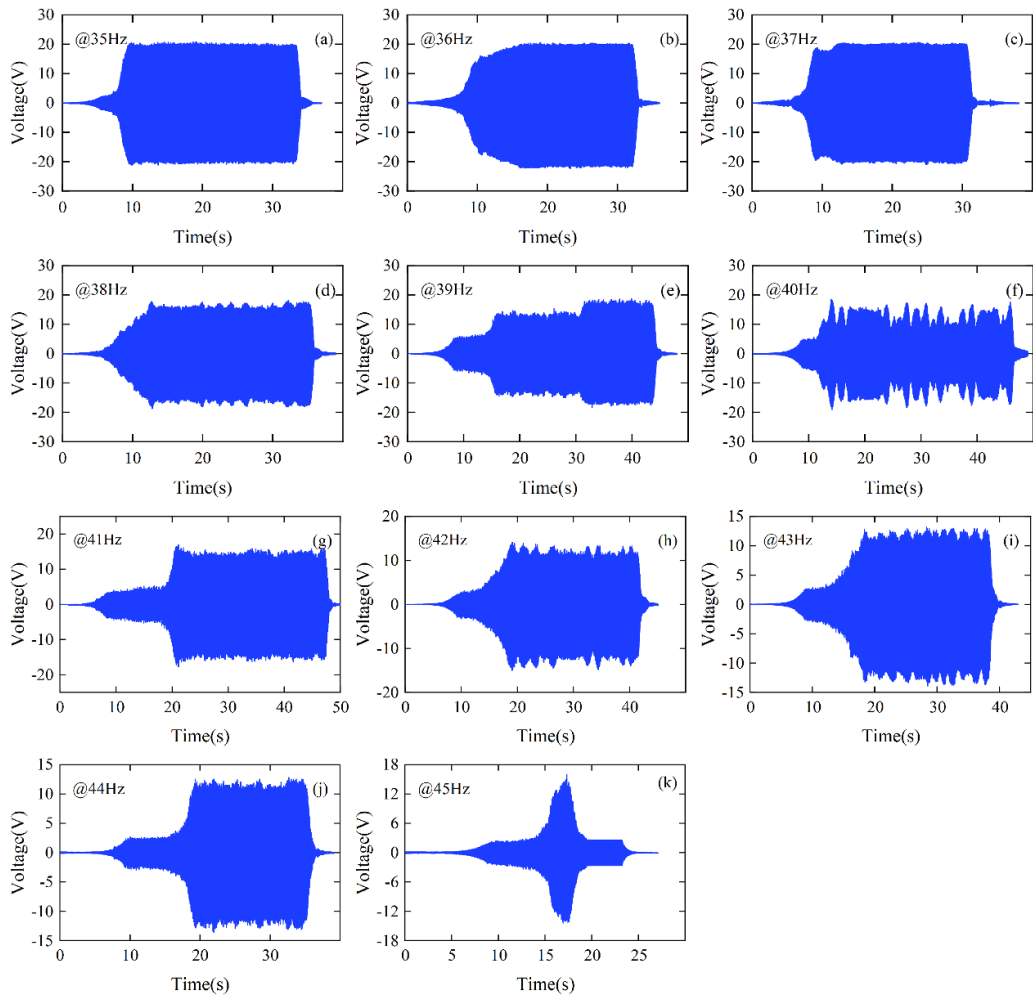
J. Phys. D: Appl. Phys. **56** (2023) 284001

Y Huang *et al*

Figure 11. Voltage output responses of the proposed LSA-PEH when the excitation frequency varies from 35 Hz to 45 Hz.

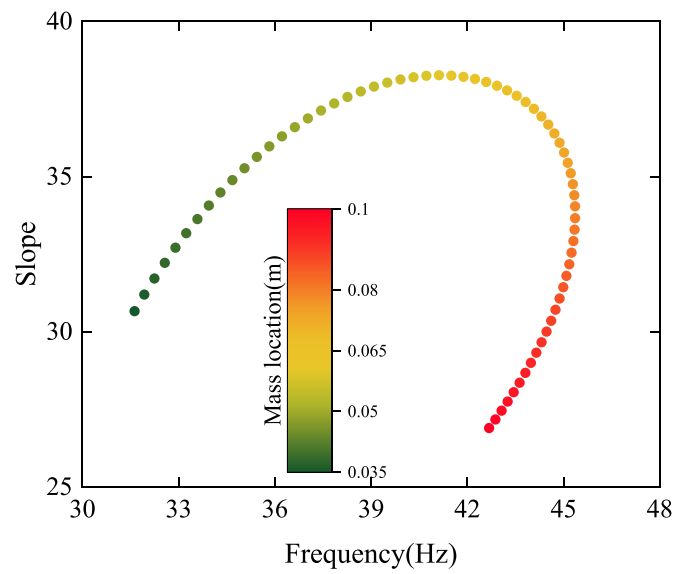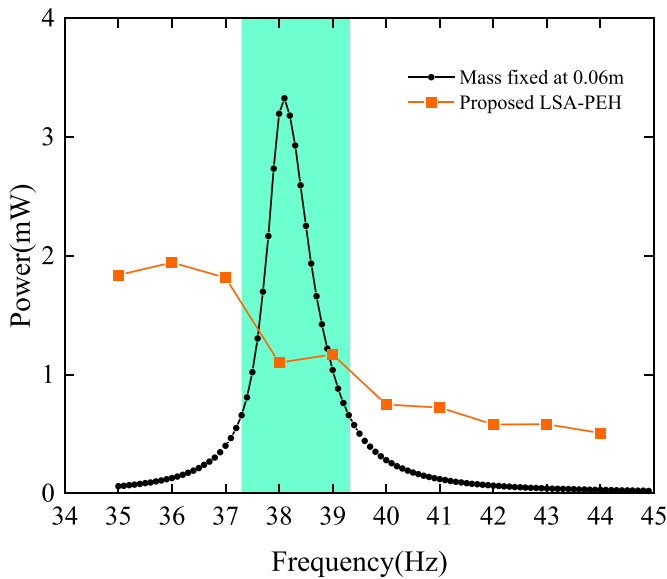**Figure 12.** The slope of the auxiliary beam at the slider fixed position versus the resonant frequency.

J. Phys. D: Appl. Phys. **56** (2023) 284001

Y Huang *et al*

Figure 13. Experimentally measured power outputs from the proposed LSA-PEH and the conventional L-shaped beam harvester with a mass fixed at 0.06 m.

In terms of the bandwidth, the conventional L-shaped PEH exhibits a narrow bandwidth around the second resonant frequency. If 0.5 mW is set as the critical power, the operating bandwidth of the conventional L-shaped PEH is just about 2.2 Hz. The effective bandwidth of the proposed LSA-PEH is about 10 Hz by the same criteria, which indicates an increase of more than 350%.

5. Conclusions

This paper has reported an LSA-PEH to realize broadband energy harvesting from ambient vibrations. A theoretical model has been built to reveal the dynamic characteristics of the proposed LSA-PEH. The relationship between the resonant frequency of the LSA-PEH and its slider position has been revealed. The effect of the slider mass on the attainable range of the resonant frequency has been investigated. Moreover, the maximum resonant frequency that the LSA-PEH can achieve has been determined to be 45.3 Hz which can be realized by placing the slider at the nodal point. The experimental results are basically in good agreement with the theoretical predictions. An abnormal phenomenon observed in the experiment is that when the excitation frequency was set at 40 Hz, the slider moved back and forth around the expected position. Based on the theoretical model, by investigating the slope of the beam at the slider stopping position, we have found that the inclination angle of the slider reached the maximum at 40 Hz, which reasonably explains the position varying behavior of the slide. In general, the experimental study has shown that the LSA-PEH can automatically adjust its resonant frequency and maintain resonance over a wide frequency range. Compared to a conventional L-shaped beam harvester, the bandwidth of the proposed LSA-PEH has been increased by 350%.

Data availability statement

The data that support the findings of this study are available upon reasonable request from the authors.

Acknowledgments

Appendix

$$\mathbf{H}_1 = \begin{bmatrix} 1 & 0 & 1 & 0 & 0 & 0 & 0 \\ 0 & 1 & 0 & 1 & 0 & 0 & 0 \\ 0 & 0 & 0 & 0 & 0 & 0 & 0 \\ 0 & 0 & 0 & 0 & \cosh(\alpha_2(L_2-s)) & \sinh(\alpha_2(L_2-s)) & -\cos(\alpha_2(L_2-s)) \\ 0 & 0 & 0 & 0 & \sinh(\alpha_2(L_2-s)) & \cosh(\alpha_2(L_2-s)) & \sin(\alpha_2(L_2-s)) \\ \cosh(\alpha_1 L_1) & \sinh(\alpha_1 L_1) & \cos(\alpha_1 L_1) & \sin(\alpha_1 L_1) & 0 & 0 & 0 \\ 0 & 0 & 0 & 0 & 0 & 0 & 0 \end{bmatrix}$$

$$\mathbf{H}_2 = \begin{bmatrix} 0 & 0 & 0 & 0 & 0 & 0 & 0 \\ 0 & 0 & 0 & 0 & 0 & 0 & 0 \\ 0 & 0 & 0 & 0 & 0 & 1 & 0 \\ -\sin(\alpha_2(L_2-s)) & 0 & 0 & 0 & 0 & 0 & 0 \\ -\cos(\alpha_2(L_2-s)) & 0 & 0 & 0 & 0 & 0 & 0 \\ 0 & -1 & 0 & -1 & 0 & 0 & 0 \\ 0 & 0 & \alpha_2 & 0 & \alpha_2 & -\cos(\beta L_1) & -\sin(\beta L_1) \end{bmatrix}$$

$$\mathbf{H}_3 = \begin{bmatrix} 0 & 0 & 0 & 0 & E_2 I_2 & 0 & -E_2 I_2 \\ \cosh(\alpha_1 L_1) & \sinh(\alpha_1 L_1) & -\cos(\alpha_1 L_1) & -\sin(\alpha_1 L_1) & 0 & 0 & 0 \\ \alpha_1^3 E_1 I_1 \sinh(\alpha_1 L_1) & \alpha_1^3 E_1 I_1 \cosh(\alpha_1 L_1) & \alpha_1^3 E_1 I_1 \sin(\alpha_1 L_1) & -\alpha_1^3 E_1 I_1 \cos(\alpha_1 L_1) & 0 & 0 & 0 \\ 0 & 0 & 0 & 0 & 1 & 0 & 1 \\ 0 & 0 & 0 & 0 & 0 & 1 & 0 \\ 0 & 0 & 0 & 0 & 1 & 0 & -1 \\ 0 & 0 & 0 & 0 & \frac{m\omega^2}{E_2 I_2} & -\alpha_2^3 & \frac{m\omega^2}{E_2 I_2} \end{bmatrix}$$

$$\mathbf{H}_4 = \begin{bmatrix} 0 & 0 & 0 & 0 & 0 & G_1 I_{\mathrm{p}}\beta\sin(\beta L_2) & -G_1 I_{\mathrm{p}}\beta\cos(\beta L_2) \\ 0 & 0 & 0 & 0 & 0 & 0 & 0 \\ 0 & 0 & -E_2 I_2 \alpha_2^3 & 0 & E_2 I_2 \alpha_2^3 & 0 & 0 \\ 0 & -\cosh(\alpha_2 s) & -\sinh(\alpha_2 s) & -\cos(\alpha_2 s) & -\sin(\alpha_2 s) & 0 & 0 \\ 1 & -\sinh(\alpha_2 s) & -\cosh(\alpha_2 s) & \sin(\alpha_2 s) & -\cos(\alpha_2 s) & 0 & 0 \\ 0 & -\cosh(\alpha_2 s) & -\sinh(\alpha_2 s) & \cos(\alpha_2 s) & \sin(\alpha_2 s) & 0 & 0 \\ \alpha_2^3 & \alpha_2^3 \sinh(\alpha_2 s) & \alpha_2^3 \cosh(\alpha_2 s) & \alpha_2^3 \sin(\alpha_2 s) & -\alpha_2^3 \cos(\alpha_2 s) & 0 & 0 \end{bmatrix}.$$

ORCID iDs

Yi Huang ⬡ https://orcid.org/0000-0002-7494-4771
Guobiao Hu ⬡ https://orcid.org/0000-0002-1288-7564
Baoping Tang ⬡ https://orcid.org/0000-0002-8286-8860
Xiaojing Mu ⬡ https://orcid.org/0000-0003-2024-2595
Yaowen Yang ⬡ https://orcid.org/0000-0002-2549-5973

References

[1] Tang X, Wang X, Cattley R, Gu F and Ball A D 2018 Energy harvesting technologies for achieving self-powered wireless sensor networks in machine condition monitoring: a review *Sensors* **18** 4113

[2] Lu S, Zhou P, Wang X, Liu Y, Liu F and Zhao J 2018 Condition monitoring and fault diagnosis of motor bearings using undersampled vibration signals from a wireless sensor network *J. Sound Vib.* **414** 81–96

[3] Shu T, Chen J, Bhargava V K and de Silva C W 2019 An energy-efficient dual prediction scheme using LMS filter and LSTM in wireless sensor networks for environment monitoring *IEEE Internet Things J.* **6** 6736–47

[4] Kalaivaani P and Krishnamoorthi R 2020 Design and implementation of low power bio signal sensors for wireless body sensing network applications *Microprocess. Microsyst.* **79** 103271

[5] Huang Y, Tang B, Deng L and Zhao C 2020 Fuzzy analytic hierarchy process-based balanced topology control of wireless sensor networks for machine vibration monitoring *IEEE Sens. J.* **20** 8256–64

[6] Han G, Zhou Z, Zhang Y, Martínez-García M, Peng Y and Xie L 2021 Sleep-scheduling-based hierarchical data collection algorithm for gliders in underwater acoustic sensor networks *IEEE Trans. Veh. Technol.* **70** 9466–79

J. Phys. D: Appl. Phys. **56** (2023) 284001

Y Huang *et al*

[7] Wang L, Zhao L, Luo G, Zhao Y, Yang P, Jiang Z and Maeda R 2020 System level design of wireless sensor node powered by piezoelectric vibration energy harvesting *Sens. Actuators* A **310** 112039

[8] Chamanian S, Baghaee S, Uluşan H, Zorlu Ö, Uysal-Biyikoglu E and Külah H 2019 Implementation of energy-neutral operation on vibration energy harvesting WSN *IEEE Sens. J.* **19** 3092–9

[9] Paul K, Amann A and Roy S 2021 Tapered nonlinear vibration energy harvester for powering Internet of Things *Appl. Energy* **283** 116267

[10] Kim T, Ko Y, Yoo C, Choi B, Han S and Kim N 2020 Design optimisation of wide-band piezoelectric energy harvesters for self-powered devices *Energy Convers. Manage.* **225** 113443

[11] Xiao H, Wang X and John S 2016 A multi-degree of freedom piezoelectric vibration energy harvester with piezoelectric elements inserted between two nearby oscillators *Mech. Syst. Signal Process.* **68** 138–54

[12] Li X, Yu K, Upadrashta D and Yang Y 2019 Comparative study of core materials and multi-degree-of-freedom sandwich piezoelectric energy harvester with inner cantilevered beams *J. Phys. D: Appl. Phys.* **52** 235501

[13] Zou D, Liu G, Rao Z, Tan T, Zhang W and Liao W-H 2021 A device capable of customizing nonlinear forces for vibration energy harvesting, vibration isolation, and nonlinear energy sink *Mech. Syst. Signal Process.* **147** 107101

[14] Haghighi E F, Ziaei-Rad S and Nahvi H 2021 Energy harvesting from a nonlinear magnet-piezoelectric multi-frequency converter array *Smart Mater. Struct.* **30** 105028

[15] Xie Z, Wang T, Kwuimy C K, Shao Y and Huang W 2019 Design, analysis and experimental study of a T-shaped piezoelectric energy harvester with internal resonance *Smart Mater. Struct.* **28** 085027

[16] Miller L M, Pillatsch P, Halvorsen E, Wright P K, Yeatman E M and Holmes A S 2013 Experimental passive self-tuning behavior of a beam resonator with sliding proof mass *J. Sound Vib.* **332** 7142–52

[17] Lan C, Chen Z, Hu G, Liao Y and Qin W 2021 Achieve frequency-self-tracking energy harvesting using a passively adaptive cantilever beam *Mech. Syst. Signal Process.* **156** 107672

[18] Abdelkefi A, Najar F, Nayfeh A and Ayed S B 2011 An energy harvester using piezoelectric cantilever beams undergoing coupled bending–torsion vibrations *Smart Mater. Struct.* **20** 115007

[19] Nie X, Tan T, Yan Z, Yan Z and Hajj M R 2019 Broadband and high-efficient L-shaped piezoelectric energy harvester based on internal resonance *Int. J. Mech. Sci.* **159** 287–305

[20] Li H, Liu D, Wang J, Shang X and Hajj M R 2020 Broadband bimorph piezoelectric energy harvesting by exploiting bending-torsion of L-shaped structure *Energy Convers. Manage.* **206** 112503

[21] Yao M, Liu P, Ma L, Wang H and Zhang W 2020 Experimental study on broadband bistable energy harvester with L-shaped piezoelectric cantilever beam *Acta Mech. Sin.* **36** 557–77

[22] Cao Y, Cao D, He G, Ge X and Hao Y 2021 Vibration analysis and distributed piezoelectric energy harvester design for the L-shaped beam *Eur. J. Mech.* A **87** 104214

[23] Yu L, Tang L and Yang T 2019 Experimental investigation of a passive self-tuning resonator based on a beam-slider structure *Acta Mech. Sin.* **35** 1079–92